International Journal of Mathematical, Engineering and Management Sciences
Vol. 11, No. 1, 269-294, 2026
https://doi.org/10.33889/IJMEMS.2026.11.1.012

# A Novel Numerical Method to Solve the Generalized Burgers-Huxley Equation

**Simran Sahlot**
Department of Mathematics,
Lovely Professional University, Phagwara, Punjab, India.
E-mail: sim.sahlot@gmail.com

**Geeta Arora**
Department of Mathematics,
Lovely Professional University, Phagwara, Punjab, India.
*Corresponding author*: geetadma@gmail.com

(Received on June 21, 2025; Revised on August 12, 2025 & October 16, 2025; Accepted on November 13, 2025)

**Abstract**
This study introduces a computational method to solve the generalized Burgers-Huxley equation which is an equation describing how diffusion, convection, and reaction work in nonlinear wave phenomena. The proposed method involves the exponential B-spline basis function along with the differential quadrature method. The method has good efficiency and accurately presents the behavior of the nonlinear partial differential equations. Ten cases are tested to demonstrate the accuracy of the numerical solution with the exact solutions supported by consistently small $L_2$ and $L_\infty$ error. The results show that the method works well and can be applied to solve similar time-dependent nonlinear equations. The present scheme can be further implemented to the higher-dimensional partial differential equations to ensure the efficiency of the scheme in handling the non-linear equations.

**Keywords-** Generalized Burgers–Huxley equation, Differential quadrature method, Exponential B-spline, Mathematical biology, Fluid dynamics.

**Abbreviations**

| | |
|---|---|
| DQM | Differential Quadrature Method |
| EB | Exponential B-spline |
| GBHE | Generalized Burgers–Huxley Equation |
| ODE | Ordinary Differential Equation |
| PDE | Partial Differential Equation |
| SSP-RK43 | Strong Stability-Preserving Runge–Kutta Method of Order 4(3) |

## 1. Introduction

Nonlinear wave phenomena are commonly observed in many branches of science and engineering, including fluid dynamics (Sánchez-Pérez et al., 2023), population biology (Macías-Díaz, 2018), combustion theory (Kwatra et al., 2025), and nerve pulse propagation (Macías-Díaz, 2014). These phenomena demonstrate the complex interactions among reaction, diffusion, and convection processes that requires the involvement of the mathematical models that can accurately depict the relationship among the parameters involve and their effects. One of the models to study these kinds of systems is the generalized Burgers–Huxley equation (GBHE) (Estevez and Gordoa, 1990). This equation presents the relation and effect of the process of convection, diffusion, and the involvement and role of the nonlinear reaction terms. The GBHE is a broader form of the Burgers' equation (Webb and McKenzie, 1984), which effectively study the turbulence and shock waves, and the Huxley equation (Cronin, 1900) which describes nonlinear reaction terms in biological and chemical processes. This equation provides the application of the involved systems

across various applications. The generalized Burgers–Huxley equation can be defined as:

$$u_t + \alpha u^{\delta} ux = \mu u_{xx} + \beta u(1 - u^{\delta})(u^{\delta} - \gamma),\ 0 < \gamma < 1 \quad (1)$$

The variables and parameters appearing in the equation can be defined as follows:
$u(x, t)$ represents the wave profile, $\alpha$ is a nonlinear convection coefficient, μ is a diffusion coefficient (viscosity), $\beta$ depicts the reaction rate, $\gamma$ is used for the threshold parameter value $(0 < \gamma < 1)$, $\delta$ represents the power-law exponent (typically considered as $\delta = 1$).

The GBHE is a nonlinear PDE that provides restricted solution due to the presence of complex boundary conditions along with the involvement of the nonlinear terms. Thus, obtaining an approximate numerical solution is required for depicting the behavior of the systems represented by this equation.

It is a multiscale equation that provides challenges to be solved numerically. This signifies the requirement of an effective numerical technique that can handle nonlinear equations. The present study employs the differential quadrature method (DQM) proposed by Bellman et al. (1972) along with the exponential B-spline (EB) basis functions presented by McCartin (1991) in his studies.

DQM is a well-known method to solve the PDEs including nonlinear elements. The obtained numerical solutions demonstrate significantly enhanced accuracy and stability with the application of the EB basis functions which are proficient in handling the nonlinearities. This method efficiently simulates dynamic systems motivated by reaction-diffusion-convection equation that produce extremely accurate results with few grid points. The proposed approach is capable to address the complex and nonlinear problems with high accuracy and speed. The different cases discussed in the manuscript provide valuable insights into the functioning of the systems represented by the GBHE.

### 1.1 Organization of the Article

The manuscript is arranged in the sections as follows: After introduction in the Section 1, the Section 2 provides the discussion on the available numerical methods in literature that are utilized to solve the well-known partial differential equations along with the GBHE. It also provides the details of the application of the differential quadrature method and the various B-spline forms involved. In Section 3, formulation of EB is provided along with the derivation of weighting coefficients for spatial derivatives. Section 4 presents the discussion on the method stability of GBHE. Section 5 presents the numerical examples with the different set of parameters to assess the accuracy and efficiency of the proposed method along with the comparisons of results with the existing methods. In Section 6, discussion is provided for the different cases for the obtained results while Section 7 describes the potential implications. Section 8 concludes the present study with the outlines of the future prospective of the research in Section 9.

## 2. Literature Review

The GBHE has been extensively studied via both analytical and numerical methods because of the presence of nonlinear terms, and it has been used to model various systems involving reactions, diffusion, and convection. Researchers have developed the use of the tanh method to obtain exact solutions for particular parameter controls (Wang et al., 1990). The travelling wave solutions for different forms of the Burgers' equation such as Burgers' equation, Burgers–KdV equation, and the Burgers–Huxley equations have been obtained by Wazwaz implementing several exact methods (Wazwaz, 2005). The Adomian decomposition method (ADM) has been implemented to handle the nonlinear terms of the Burgers–Huxley and Burgers–Fisher equations by Ismail et al. (2004). A novel Taylor wavelet method (TWM) for solving the GBHE has been proposed that results in efficient results by Korkut (2023). The results of the proposed approach have

been compared with several existing approaches and presented as an effective method for solving nonlinear reaction–diffusion systems.

Appadu and Tijani (2022) have implemented the nonstandard finite difference (NSFD) methods to find the numerical solution of the GBHE for a defined of initial and boundary conditions. The application of the Galerkin method has been presented to solve the GBHE and Huxley equations by Kumar et al. (2022) and comparing the obtained results with the mesh free neural network approach. Many of the well-known schemes along with the finite difference method have shown the application of the quasi linearization to deal with the nonlinear terms and thus reducing it in a linear form for the efficiently calculating the numerical solution (Kabeto et al., 2024). Mohan and Khan (2021) studied the GBHE with the novel form of Galerkin approach to show the existence of the weak solutions. Wang (2021) has highlighted the limitations of the traditional smooth approach in modelling complex phenomena and emphasized the importance of using non-smooth formulations, such as the GBHE with fractal derivatives.

B-spline basis function has been successfully implemented to solve differential equations of various forms implementing the different quadrature method. The modified proposed by the researchers has further enhanced the accuracy that negates the challenge appearing at the boundary and the ill conditioned matrix system. The cubic B-spline differential quadrature method with modified basis functions (MCB-DQM) has been presented by Singh et al. (2016) to solve the GBHE. The proposed method reduced the PDE into a set of ordinary differential equations (ODEs) and hence employing the SSP-RK43 scheme, which is a version combining the tradition Runge Kutta method of order three and four with a set of coefficients. The results demonstrated that DQM resulted in less errors on coarse grid in comparison to refined grid required in the finite difference method.

The finite difference approach and the DQM is presented in a comparable form by Aziz et al. to solve the Burger's equation, for the different number of nodes (Aziz et al., 2019). The results presented in this paper shows that DQM give better accuracy in comparison to the finite difference method. Aswin and Awasthi (2019) presented a polynomial-based DQM to solve the convection–diffusion–reaction equation numerically. The method was applied to the Newell–Whitehead equation, Burgers–Fisher equation, and Burgers–Huxley equation to present a comparison of the obtained results with the published results. Thus, the method is verified in the literature by various researchers by comparing the errors with the methods already applied to solve the differential equation. This paper introduces an innovative framework utilizing DQM with EBs to provide high precision solutions, establishing the method for both accuracy and stability in solving nonlinear PDEs.

## 3. Method Description

The quadrature methods have been utilized in literature to handle the partial differential equations efficiently. The proposed method involves the combination of differential quadrature approach with the exponential basis functions. The approximation of the derivatives in the DQM transform the considered PDE into a system of first-order ordinary differential equations (ODEs) utilizing spline-based weighting coefficients. The ODE this obtained is then solved implementing the strong stability preserving Runge–Kutta method (SSP-RK43) to ensure stability. The accuracy of the proposed method is confirmed through different ten cases that confirms its efficiency in capturing the dynamics of the system.

### 3.1 Differential Quadrature Method

Bellman and his team developed a well-known method, DQM which is known to be easy and effective at solving many kinds of differential equations (Bellman et al., 1972). DQM locates the derivatives at specific points by giving different weights to the function values across the domain. This feature makes the method

extremely useful for solving PDEs which shows that it is suitable in handling engineering problem (Arora and Joshi, 2016; Arora et al., 2023).

### 3.1.1 Domain Discretization and Derivative Approximation

Let the spatial domain [*a*, *b*] be divided into *N* equally spaced nodes as follows:
$a = x_0 < x_1 < x_2 < \cdots < x_N = b,$

with uniform spacing $h = \frac{b-a}{N}$.

At each node $x_i$, the $r^{th}$order derivative of a function $u(x)$is approximated using DQM by:
$\frac{d^r u}{dx^r}\Big|_{x_i} \approx \sum_{j=0}^{N} W_{ij}^r u(x_j) r = 1,2, \ldots$ (2)

where, $W_{ij}^r$ denotes the weighting coefficients corresponding to the $r^{th}$ derivative.

### 3.1.2 First and Second Derivative Weights

DQM approximates the first derivative of $u(x)$ at a given point $x(i)$ by computing a weighted sum of the function values at the neighboring grid points. The weights are determined based on the grid configuration and the chosen derivative approximation method.
$\frac{d^r u}{dx^r}\Big|_{x_i} \approx \sum_{j=0}^{N} W_{ij}^{(1)} u(x_j)$ (3)

Once the first derivative weights $W_{ij}^{(1)}$ are computed, the second derivative weights $W_{ij}^{(2)}$ are derived by considering the spatial differences between neighboring points. These are calculated by applying finite difference approximations, using the first derivative weights and adjusting for the grid spacing as follows:
$W_{ij}^{(2)} = 2W_{ij}^{(1)}\left(W_{ii}^{(1)} - \frac{1}{(x_i - x_j)}\right), \qquad i \neq j$ (4)

$W_{ii}^{(2)} = -\sum_{j=0, j\neq 1}^{N} W_{ij}^{(2)}$ (5)

## 3.2 Exponential B-Splines

The B-spline basis functions are the well-known basis functions for its smoothness and ability to handle the complex form of the differential equations. The B-spline basis functions exist in different forms such as exponential, trigonometric, hyperbolic form. These basis functions are successfully implemented with DQM to solve various equations in its linear and nonlinear forms. The exponential splines are the extended polynomial B-splines involving an adjustable parameter λ, which enhances its applicability to approximate the complex solutions. The third-degree EB-spline (Rani et al., 2023) has been recently utilized to solve the one-dimensional nonlinear Schrodinger equation in combination with the PSO algorithm for the parameter λ. In this study, the optimal λ is considered as 1 in each case for simplicity.

The third-degree EB-spline $B_m(x)$ is defined as:

$$B_m(x) = \left(\frac{1}{h^3}\right)\begin{cases} \mu(x_{m-2} - x) - \frac{\mu}{\lambda}\left[\sinh\left(\lambda(x_{m-2} - x)\right)\right], & x \in [x_{m-2}, x_{m-1}], \\ \eta_1 + \mu_1(x_m - x) + \xi_1 e^{\lambda(x_m - x)} + \zeta_1 e^{-\lambda(x_m - x)}, & x \in [x_{m-1}, x_m], \\ \eta_1 + \mu_1(x_m - x) + \xi_1 e^{\lambda(x - x_m)} + \zeta_1 e^{-\lambda(x - x_m)}, & x \in [x_m, x_{m+1}], \\ \mu(x - x_{m+2}) - \frac{\mu}{\lambda}\left[\sinh\left(\lambda(x - x_{m+2})\right)\right], & x \in [x_{m+1}, x_{m+2}] \end{cases}$$

Here, $\lambda$ is the exponential parameter, $h = \frac{b-a}{n}$ is the uniform spacing, and the constants are:

$\eta^1 = \frac{(\lambda h\, cosh(\lambda h))}{(\lambda h\, cosh(\lambda h) - sinh(\lambda h))}$,

$\mu^1 = \frac{[\lambda^2 cosh^2(\lambda h) + sinh^2(\lambda h)]}{[(\lambda h\, cosh(\lambda h) - sinh(\lambda h))(1 - cosh(\lambda h))]}$,

$\mu = \frac{\lambda}{(2\lambda h\, cosh(\lambda h) - sinh(\lambda h))}$,

$\xi_1 = \frac{1}{4}\frac{[(1 - cosh(\lambda h) + sinh(\lambda h))e^{\{-\lambda h\}} - sinh(\lambda h)]}{[(\lambda h\, cosh(\lambda h) - sinh(\lambda h))(1 - cosh(\lambda h))]}$, and

$\zeta_1 = \frac{1}{4}\frac{[(-1 + cosh(\lambda h) + sinh(\lambda h))e^{\{\lambda h\}} - sinh(\lambda h)]}{[(\lambda h \cosh(\lambda h) - \sinh(\lambda h))(1 - \cosh(\lambda h))]}$.

The function values and derivatives at nodal points are given in (Rani et al., 2024):

$B_m(x_{m-1}) = B_m(x_{m+1}) = \alpha,\ B_m(x_m) = 1,$

$B'_m(x_{m-1}) = -B'_m(x_{m+1}) = \beta,\ B'_m(x_m) = 0,$

$B''_m(x_{m-1}) = B''_m(x_{m+1}) = \gamma,\ B''_m(x_m) = -\gamma.$

where,

$\alpha = \frac{(sinh(\lambda h) - \lambda h)}{(2\lambda h\, cosh(\lambda h) - sinh(\lambda h))}$,

$\beta = \frac{(\lambda\, cosh(\lambda h) - 1)}{(2\lambda h\, cosh(\lambda h) - sinh(\lambda h))}$,

$\gamma = \frac{\left(\lambda^2 sinh(\lambda h)\right)}{2\lambda h\, cosh(\lambda h) - sinh(\lambda h)}$.

To ensure diagonal dominance in the system matrix, the boundary functions are modified as:

$M_1(x) = B_1(x) + 2B_0(x),$

$M_2(x) = B_2(x) - B_0(x),$

$M_j(x) = B_j(x),\ j = 3, \ldots, N-2,$

$M_{N-1}(x) = B_{N-1}(x) - B_{N+1}(x)$, and

$M_N(x) = B_N(x) + 2B_{N+1}(x).$

***Calculation of weighting coefficients*:**

The weighting coefficients for the first derivative are obtained by solving the linear system:

$MQ(1) = F,$

where, *M* is the coefficient matrix formed by evaluating the EBs as basic functions at the nodal points, *F* is the right-hand side vector, and $Q(1)$ represents the vector of first derivative weights. Owing to the local support of the EB functions (Mangal and Gupta, 2025), the resulting system yields a tridiagonal matrix in the form:

$$\begin{bmatrix} 1+2\alpha & \alpha & 0 & \dots & \dots & 0 \\ 0 & 1 & \alpha & 0 & \dots & \vdots \\ 0 & \alpha & 1 & \alpha & \dots & 0 \\ 0 & 0 & \alpha & 1 & \ddots & \vdots \\ \vdots & \ddots & \ddots & \ddots & \ddots & \alpha \\ \vdots & \ddots & 0 & \alpha & 1 & \alpha \\ 0 & \dots & \dots & 0 & \alpha & 1+2\alpha \end{bmatrix} \begin{bmatrix} a_{11} \\ a_{12} \\ \vdots \\ \vdots \\ a_{1N-1} \\ a_{1N} \end{bmatrix} = \begin{bmatrix} -2\beta \\ 2\beta \\ 0 \\ \vdots \\ \vdots \\ 0 \\ 0 \end{bmatrix}$$

This tridiagonal system is efficiently solved via the Thomas algorithm, which yields the coefficients $a_{11}, a_{12}, \dots a_{1N}$. Similar systems are formulated and solved for each remaining knot point to determine the complete set of weighting coefficients for the first derivative Equation (3).

The evaluations of the EB function $B_m(x)$ and its first and second derivatives shown in Equations (4) and (5) at the surrounding nodes, are presented in **Table 1**.

**Table 1.** Values of the exponential B-spline and its derivatives at nodal points.

| | $x_{m-2}$ | $x_{m-1}$ | $x_m$ | $x_{m+1}$ | $x_{m+2}$ |
|---|---|---|---|---|---|
| $B_{m(x)}$ | 0 | $\alpha$ | 1 | $\alpha$ | 0 |
| $B'_{m(x)}$ | 0 | $\beta$ | 0 | $-\beta$ | 0 |
| $B''_{m(x)}$ | 0 | $\gamma$ | $-\gamma$ | $\gamma$ | 0 |

## 4. Stability Analysis

The stability of a numerical scheme is essential to ensure that numerical errors or perturbations do not grow uncontrollably during computations. In this study, the stability of the proposed EB-DQM combined with SSP- RK43 is investigated. The analysis focuses on eigenvalue examination of the semi-discretized system obtained from spatial discretization.

### 4.1 Semi-Discretization and Linearization

Applying EB-DQM for spatial discretization to the GBHE

$u_t + \alpha u u_x - u_{xx} = \beta u(1-u)(u-\gamma), \quad x \in [a,b], t > 0,$

yields a semi-discrete system of ODEs:

$\frac{d\boldsymbol{U}}{dt} = \boldsymbol{F}(\boldsymbol{U})$.

where, $\boldsymbol{U}$ denotes the vector of approximate solution values at the grid points, and $\boldsymbol{F}(\boldsymbol{U})$ represents the spatially discretized nonlinear terms.

Linearizing $\boldsymbol{F}(\boldsymbol{U})$ about a steady-state solution $\boldsymbol{U}^*$ gives

$\frac{d\delta\boldsymbol{U}}{dt} = \boldsymbol{J}\delta\boldsymbol{U}$.

where, $\delta\boldsymbol{U} = \boldsymbol{U} - \boldsymbol{U}^*$ and $\boldsymbol{J}$ is the Jacobian matrix of $\boldsymbol{F}(\boldsymbol{U})$ evaluated at :

$\boldsymbol{J} = -\alpha\boldsymbol{U}^*\boldsymbol{D}x + \boldsymbol{D}xx$.

Here, $\boldsymbol{D}_x$ and $\boldsymbol{D}_{xx}$ represent the first and second derivative weighting co-efficient matrices derived using EB-DQM.

### 4.2 Eigenvalue Spectrum and Stability Region

The solution of the linearized system is expressed as
$\delta \boldsymbol{U}(t) = \sum_j c_j e^{\lambda_j t} \boldsymbol{v}j$ .

where, $\lambda_j$ and $\boldsymbol{v}_j$ denote the eigenvalues and eigenvectors of $\boldsymbol{J}$, respectively. Stability of the semi-discretized system requires all $\lambda_j$ to lie in the left half of the complex plane where $\lambda_j$ and $\boldsymbol{v}_j$ denote the eigenvalues and eigenvectors of $\boldsymbol{J}$, respectively. Stability of the semi-discretized system requires all $\lambda_j$ to lie in the left half of the complex plane (Arora and Joshi, 2018; Kapoor, 2023).

### 4.3 Time Integration and Amplification Factor

In the temporal discretization, SSP-RK43 advances the solution as
$U^{n+1} = G(\mu_j)U^n$,

where, $\mu_j = k\lambda_j$ with $k$ being the time step, and $G(\mu_j)$ is the amplification factor of SSP-RK43:
$G(\mu) = 1 + \mu + \frac{1}{2}\mu^2 + \frac{1}{6}\mu^3$.

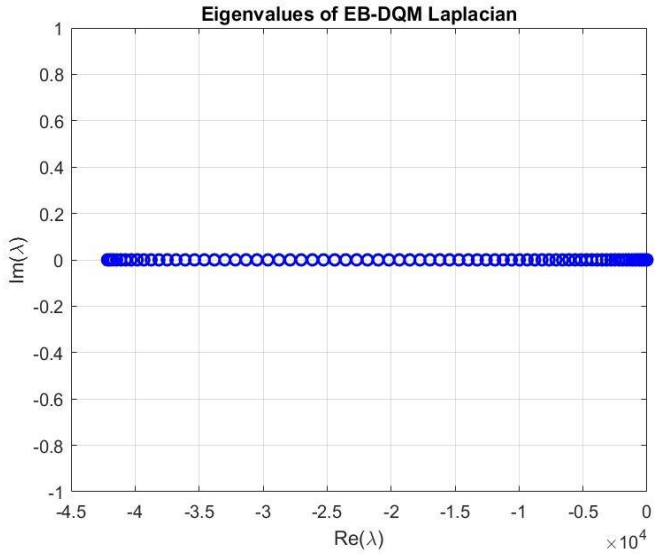


**Figure 1.** Eigenvalue spectrum of the Jacobian matrix J obtained from EB- DQ.

The scheme remains stable if

$$|G(\mu_j)| \leq 1, \quad \forall j.$$

The eigenvalues $\lambda j$ of $\boldsymbol{J}$ are calculated numerically in MATLAB. Since $\boldsymbol{D}_{xx}$ is a negative semi-definite matrix, all $\lambda_j$ are negative and real, which favors stability as shown in **Figure 1**. The scaled eigenvalues $\mu_j = k\lambda_j$ must reside within the absolute stability region of SSP-RK43, defined by $|G(\mu)| \leq 1$, shown in **Figure 2**.

**Figure 3** illustrates the absolute stability region of the SSP-RK43 scheme in the complex μ-plane. The solid contour represents the stability boundary $|G(\mu)| = 1$, while the interior region, marked with diagonal dot patterns, denotes the stable domain where $|G(\mu)| < 1$. The scaled eigen values $\mu_j$ of EB-DQM are represented within the stable region, confirming the stability of the method for the selected time step $k$.

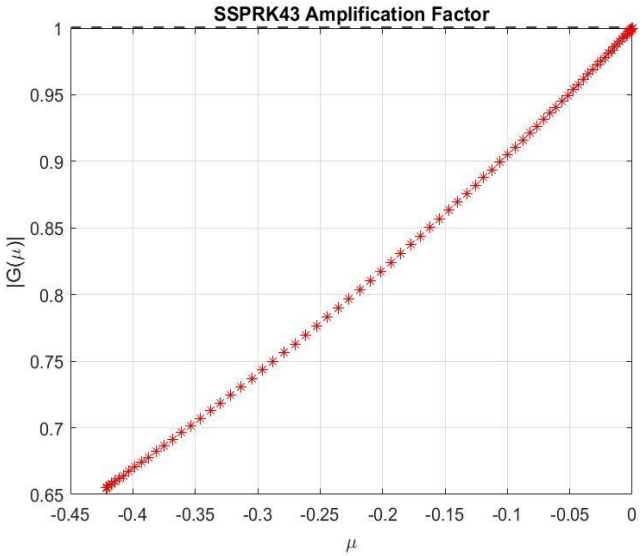


**Figure 2.** Amplification factor $|G(\mu)|$ of SSPRK43 versus $\mu = k\lambda$. Stability is ensured for $|G(\mu)| \leq 1$.

## 4.4 Spectral Radius and Time Step Restriction

The spectral radius of the Jacobian matrix denoted as $\rho(\boldsymbol{J})$, is a key metric in assessing the stability of the numerical scheme. It represents the maximum absolute value of the eigenvalues of $\boldsymbol{J}$:
$\rho(\boldsymbol{J}) = \max_j |\lambda j|$.

In the context of EB-DQM, **J** is derived from the combination of derivative weighting matrices $\boldsymbol{D}_x, \boldsymbol{D}_{xx}$, and the linearized reaction terms. Due to the diffusive nature of the second derivative matrix $\boldsymbol{D}_{xx}$, the eigenvalues $\lambda_j$ are predominantly negative real numbers, indicating a damping effect on high-frequency error modes.

To maintain stability, the time step $k$ must be selected such that all scaled eigenvalues $\mu_j = k\lambda_j$ lie within the absolute stability region of SSP-RK43. This requirement translates to the following constraint:
$k \leq \frac{\mu_{max}}{\rho(J)}$, where $\mu_{max}$ is the maximum value of μ within the SSP-RK43 stability region, often determined from the boundary where $|G(\mu)| = 1$. For SSP-RK43, $\mu_{\max}$ is approximately $-2.0$. on the negative real axis. In this study, the computed spectral radius of $\boldsymbol{J}$ is $\rho(\boldsymbol{J}) = 1.64 \times 10^4$, and amplification factor plots in **Figure 2** visually support the conclusion that all eigenvalues remain within the stability region of SSP-RK43. This ensures that the combined EB-DQM and SSP-RK43 approach effectively suppresses numerical instabilities, even for stiff terms arising in GBHE. The method is explained summarized below in Algorithm 1.

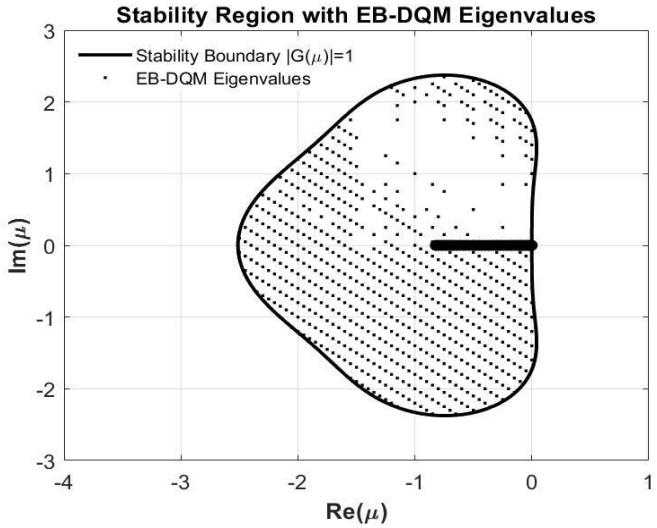


**Figure 3.** Stability region of SSP-RK43 with EB-DQM scaled eigenvalues eigen values $\mu_j$. Stability holds if all $\mu_j$ lie within the boundary $|G(\mu)| = 1$.

**Algorithm 1.** EB-DQM with SSP-RK43 for solving GBHE.

| Step | Description |
|---|---|
| 1. | Discretize the spatial domain $[a, b]$ into $N$ nodes with spacing $h$. |
| 2. | Construct exponential B-spline basis functions $B_m(x)$ with exponential parameter $\lambda$. |
| 3. | Compute derivative weighting coefficients $A_{ij}$ *and* $B_{ij}$ using EB-DQM formulation. |
| 4. | Transform GBHE into semi-discrete ODE form. |
| 5. | Initialize $U(0)$ and choose time step $\Delta t$ satisfying stability conditions. |
| 6. | For each time step $n$: compute SSP-RK43 stages $k_1, k_2, k_3, k_4$ and update $U^{n+1} = U^n + \Delta t(b_1k_1 + b_2k_2 + b_3k_3 + b_4k_4)$. |
| 7. | Evaluate eigenvalues of Jacobian $J = \frac{\partial F}{\partial U}$; ensure all $Re(\lambda) < 0$ for stability. |
| 8. | Compute $L_2$ and $L_\infty$ error norms to validate accuracy against exact or benchmark results. |

***Parameters*:** Domain $[\boldsymbol{a}, \boldsymbol{b}]$ with $\boldsymbol{N}$ nodes and spacing $\boldsymbol{h} = \frac{\boldsymbol{b-a}}{\boldsymbol{N-1}}$. Exponential B-splines use tension $\boldsymbol{\lambda}$. Time stepping: SSP-RK43 with time-step $\boldsymbol{\Delta t}$ and stages $(\boldsymbol{k_1}, \boldsymbol{k_2}, \boldsymbol{k_3}, \boldsymbol{k_4})$. Stability check via Jacobian $\boldsymbol{J} = \frac{\boldsymbol{\partial F}}{\boldsymbol{\partial U}}$ and eigenvalues $\boldsymbol{\mu}$ (require $\boldsymbol{Re(\mu) < 0}$ for the chosen $\boldsymbol{\Delta t}$). Physical coefficients: convection $\boldsymbol{\alpha}$, reaction $\boldsymbol{\beta}, \boldsymbol{\gamma}$; final time $\boldsymbol{T}$.

## 5. Error Analysis and Comparison

To assess the accuracy and effectiveness of the proposed numerical scheme, a detailed comparison is performed using the $L_2$ and $L_\infty$ error norms. These norms are defined as follows

$$L_2 = \sqrt{\left(\frac{1}{N}\right) \sum_{i=1}^{N} \left|u_i^e - u_i^n\right|^2}, \text{ and}$$

$$L_\infty = \max_{1 \le i \le N} \left|u_i^e - u_i^n\right|.$$

where, $u_i^e$ and $u_i^n$ denote the exact and numerical solutions at the $i-$th grid point, respectively, and where, $N$ is the total number of spatial nodes.

## 5.1 Test Cases for the GBHE

A traveling wave solution of Equation (1) as given in (Wang et al., 1990) is expressed as:

$$u(x,t) = \left(\frac{\gamma}{2}\right)\{1 + \tanh(\kappa(x = \omega t))\}^{\frac{1}{\delta}} \quad (8)$$

where, $\omega$ and $\kappa$ represent the wave speed and wave number, respectively, and are defined below:

$$\omega = \left(\frac{\alpha\gamma}{\delta+1} - \frac{\left((1+\delta-\gamma) - \alpha + \sqrt{\alpha^2 + 4\beta(\delta+1)}\right)}{\left(2(\delta+1)\right)}\right), \text{ and}$$

$$\kappa = \frac{\gamma\delta\left(-\alpha+\sqrt{\alpha^2+4\beta(\delta+1)}\right)}{4(\delta+1)}.$$

In this study, the effectiveness of the proposed numerical method is assessed by considering ten distinct cases with various parameters, $\alpha, \beta,$ and $\gamma$. The results for Cases 1 through 8 are compared with those reported in (Appadu et al., 2019), whereas those for Case 9 are validated via the references (Appadu and Tijani, 2022; Deng, 2008) and for Case 10 are validated via the reference (Batiha et al., 2008; Bratsos, 2011; Hashim et al., 2006; Ismail et al., 2004; Singh et al., 2016).

(i) Set of parameters: $\alpha = 0.5, \beta = 0.5,$ and $\gamma = 0.001$.
(ii) Configuration where $\beta = 2.0$ surpasses $\alpha = 0.5$, diffusion remains low with $\gamma = 0.001$.
(iii) A strongly reaction-driven system defined by $\alpha = 0.5, \beta = 10.0,$ and $\gamma = 0.001$ *(highly stiff case).*
(iv) A regime with dominant advection: $\alpha = 2.0, \beta = 0.5, \gamma = 0.001$.
(v) Uniform scenario where all parameters are equal: $\alpha = \beta = \gamma = 0.5$.
(vi) Moderately diffusive case with $\gamma = 0.5, \alpha = 0.5,$ and stronger reaction coefficient $\gamma = 2.0$.
(vii) A case with enhanced nonlinearity: $\alpha = 0.5, \beta = 10.0,$ and $\gamma = 0.5$ *(reaction-dominated).*
(viii) Advection-preferred dynamics with $\alpha = 2.0, \beta = 0.5,$ and $\gamma = 0.5$.
(ix) Balanced setup where $\alpha = \beta = 1.0$, $\delta = 4$, and $\gamma = 0.01$, consistent with benchmarks in (Appadu and Tijani, 2022; Deng, 2008).
(x) Reference case adopted from (Singh et al., 2016), with $\alpha = \beta = 1.0,$ and minimal diffusion $\gamma = 0.001$.

***Case* I**

This case considers the parameter configuration $\alpha = \beta = 0.5$, $\delta = 1$, and $\gamma = 0.001$. The numerical solutions are obtained by taking spatial space length $h = 0.1$ and time-step $\Delta t = 0.001$. The precision of the present numerical method is evaluated by comparing the computed results with the exact corresponding solution at time levels $t = 1$ and $t = 10$, as reported in **Tables 2** and **3**. **Figure 4** provides two visualizations: (i) a comparative plot demonstrating the accuracy of the proposed approach and (ii) a three-dimensional surface plot that illustrates the physical behavior and temporal evolution of the solution. This illustrates the evolution of the solution profile at various time levels, where the parameters represent a balanced interplay between diffusion, reaction, and convection. The solution exhibits smooth propagation without steep gradients, indicating a stable regime dominated by diffusion. As time progresses, the solution gradually transitions towards the steady-state profile, showing no significant oscillations or shocks.

**Table 2.** Case I: comparison of numerical and exact solutions at $t = 1$ and $t = 10$.

| $t$ | $x$ | Exact (Wang et al., 1990) | **Present method** | NSFD1 | NSFD2 | EEFDM | FIEFDM |
|---|---|---|---|---|---|---|---|
| | | | | Appadu et al. (2019) | | | |
| 1 | 0.1 | 5.000858e-4 | 5.000785e-4 | 5.000764e-4 | 5.000764e-4 | 5.000768e-4 | 5.000769e-4 |
| | 0.5 | 5.001249e-4 | 5.001045e-4 | 5.000985e-4 | 5.000985e-4 | 5.000998e-4 | 5.000998e-4 |
| | 0.9 | 5.001640e-4 | 5.001566e-4 | 5.001545e-4 | 5.001545e-4 | 5.001549e-4 | 5.001549e-4 |
| 10 | 0.1 | 5.007711e-4 | 5.007638e-4 | 5.007616e-4 | 5.007616e-4 | 5.007621e-4 | 5.007621e-4 |
| | 0.5 | 5.008102e-4 | 5.007898e-4 | 5.007838e-4 | 5.007838e-4 | 5.007851e-4 | 5.007851e-4 |
| | 0.9 | 5.008492e-4 | 5.008418e-4 | 5.008397e-4 | 5.008397e-4 | 5.008402e-4 | 5.008402e-4 |

**Table 3.** Case I: $L_2$ and $L_\infty$ error norms at different time levels.

| Time | Method | $L_2$ Error | $L_\infty$ Error |
|---|---|---|---|
| 0.5 | **Present Method** | 1.4879e-8 | 2.0375e-8 |
| Appadu et al. (2019) | NSFD1 | 1.7435e-8 | 2.6417e-8 |
| | NSFD2 | 1.7435e-8 | 2.6417e-8 |
| | EEFDM | 1.6590e-8 | 2.5136e-8 |
| | FIEFDM | 1.6589e-8 | 2.5134e-8 |
| 1.0 | **Present Method** | 1.4879e-8 | 2.0375e-8 |
| Appadu et al. (2019) | NSFD1 | 1.7437e-8 | 2.6419e-8 |
| | NSFD2 | 1.7437e-8 | 2.6419e-8 |
| | EEFDM | 1.6591e-8 | 2.5138e-8 |
| | FIEFDM | 1.6590e-8 | 2.5136e-8 |

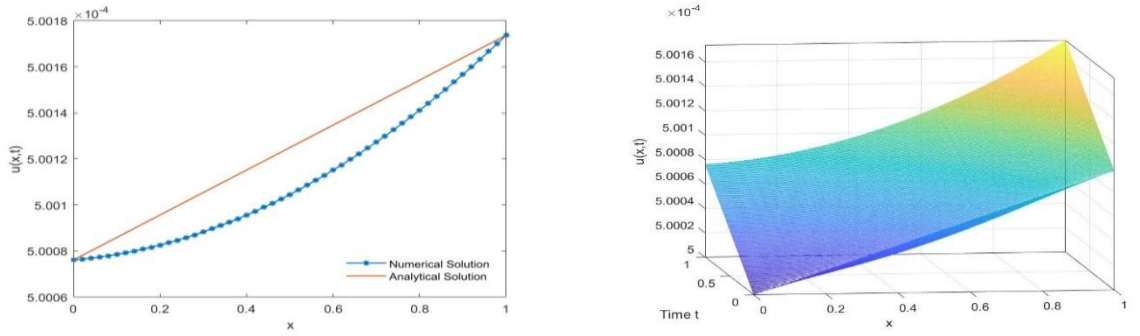


(i) (ii)

**Figure 4.** (i) Comparison of the exact and numerical solution of Case I. (ii) Numerical solution is shown by 3-D plot.

## *Case* II

This scenario considers the parameter configuration $\alpha = \beta = 0.5,\ \delta = 1,$ and $\gamma = 0.001$. The numerical solutions are obtained by taking spatial space length $h = 0.1$ and time-step $\Delta t = 0.001$. The precision of the present numerical method is evaluated by comparing the computed results with the exact corresponding solution at time levels $t = 1$ and $t = 10$, as reported in **Tables 2** and **3**. **Figure 5** provides two visualizations: (i) a comparative plot demonstrating the accuracy of the proposed approach and (ii) a three-dimensional surface plot that illustrates the physical behavior and temporal evolution of the solution. The obtained solution profile is seen as steep near the boundaries that reflect the stronger reaction dynamics.

**Table 4.** Case II: Comparison of numerical and exact solutions at $t = 1$ and $t = 10$.

| $t$ | $x$ | Exact Wang et al. (1990) | **Present method** | NSFD1 | NSFD2 | EEFDM | FIEFDM |
|---|---|---|---|---|---|---|---|
| | | | | Appadu et al. (2019) | | | |
| 1 | 0.1 | 5.0041e-4 | 5.0038e-4 | 5.0036e-4 | 5.0036e-4 | 5.0037e-4 | 5.0037e-4 |
| | 0.5 | 5.0050e-4 | 5.0041e-4 | 5.0036e-4 | 5.0036e-4 | 5.0039e-4 | 5.0039e-4 |
| | 0.9 | 5.0059e-4 | 5.0056e-4 | 5.0054e-4 | 5.0054e-4 | 5.0055e-4 | 5.0055e-4 |
| 10 | 0.1 | 5.0392e-4 | 5.0388e-4 | 5.0387e-4 | 5.0387e-4 | 5.0388e-4 | 5.0388e-4 |
| | 0.5 | 5.0404e-4 | 5.0391e-4 | 5.0387e-4 | 5.0387e-4 | 5.0389e-4 | 5.0389e-4 |
| | 0.9 | 5.0409e-4 | 5.0406e-4 | 5.0404e-4 | 5.0404e-4 | 5.0405e-4 | 5.0405e-4 |

**Table 5.** Case II: $L_2$ and $L_\infty$ error norms at $t = 1$ and $t = 10$.

| $t$ | Method | $L_2$ Error | $L_\infty$ Error |
|---|---|---|---|
| 1 | **Present method** | 6.3384e-8 | 8.6797e-8 |
| Appadu et al. (2019) | NSFD1 | 8.9678e-8 | 1.3587e-7 |
| | NSFD2 | 8.9678e-8 | 1.3587e-7 |
| | EEFDM | 7.3356e-8 | 1.1115e-7 |
| | FIEFDM | 7.3349e-8 | 1.1114e-7 |
| 10 | **Present method** | 6.3380e-8 | 8.6791e-8 |
| Appadu et al. (2019) | NSFD1 | 8.9698e-8 | 1.3591e-7 |
| | NSFD2 | 8.9697e-8 | 1.3591e-7 |
| | EEFDM | 7.3355e-8 | 1.1114e-7 |
| | FIEFDM | 7.3350e-8 | 1.1114e-7 |

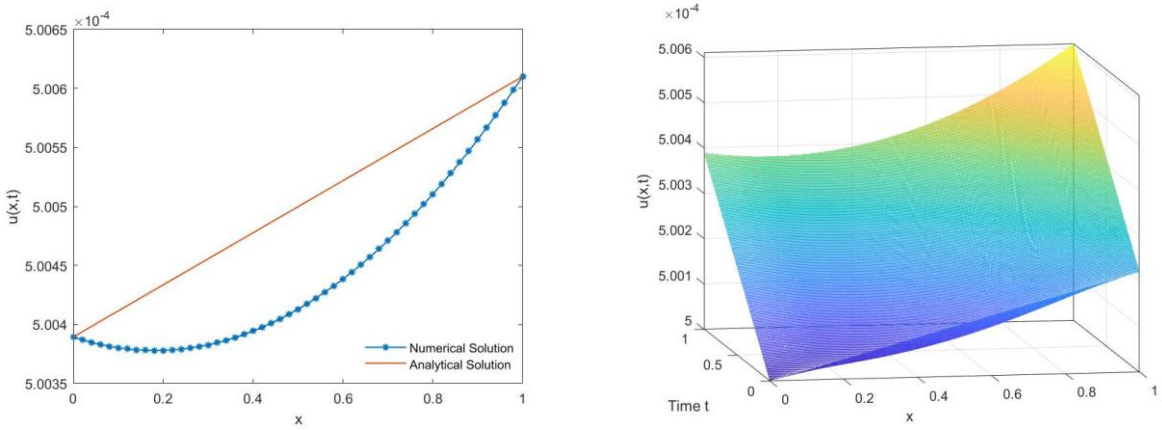


(i) (ii)

**Figure 5.** (i) Comparison of the exact and numerical solution of Case II. (ii) Numerical solution is shown by 3-D plot.

### *Case* III

In this example, the selected parameters are $\alpha = 0.5, \beta = 10,\ \delta = 1$, and $\gamma = 0.001$. The numerical solutions are obtained by taking spatial space length $h = 0.1$ and time-step $\Delta t = 0.001$. The numerical results obtained using the proposed method are compared with the exact solution at two different time levels, $t = 1$ and $t = 10$, as shown in **Tables 6** and **7**. **Figure 6** presents the results graphically: (i) a comparative curve highlighting the closeness between the numerical and exact solutions, and (ii) a 3D plot visualizing the propagation and variation of the solution over time. The figure shows the dominance of $\beta$ over $\alpha$ which produces sharp front and develop boundary layers. The method successfully resolves these steep gradients, preserving stability and accuracy even in the presence of stiff reaction terms. This validates the capability of the EB-DQM with the SSP-RK43 scheme to handle highly nonlinear regimes.

**Table 6.** Case III: comparison of numerical and exact solutions at $t$ = 1 and $t$ = 10.

| $T$ | $x$ | Exact (Wang et al., 1990) | **Present method** | NSFD1 | NSFD2 | EEFDM | FIEFDM |
|---|---|---|---|---|---|---|---|
| | | | | Appadu et al. (2019) | | | |
| 1 | 0.1 | 5.0229e-4 | 5.0212e-4 | 5.0168e-4 | 5.0168e-4 | 5.0207e-4 | 5.0207e-4 |
| | 0.5 | 5.0250e-4 | 5.0205e-4 | 5.0083e-4 | 5.0083e-4 | 5.0191e-4 | 5.0191e-4 |
| | 0.9 | 5.0271e-4 | 5.0254e-4 | 5.0211e-4 | 5.0211e-4 | 5.0250e-4 | 5.0250e-4 |
| 10 | 0.1 | 5.2238e-4 | 5.2221e-4 | 5.2176e-4 | 5.2176e-4 | 5.2217e-4 | 5.2217e-4 |
| | 0.5 | 5.2259e-4 | 5.2214e-4 | 5.2087e-4 | 5.2087e-4 | 5.2200e-4 | 5.2200e-4 |
| | 0.9 | 5.2280e-4 | 5.2264e-4 | 5.2218e-4 | 5.2218e-4 | 5.2259e-4 | 5.2259e-4 |

**Table 7.** Case III: $L_2$ and $L_\infty$ error norms at $t$ = 1 and $t$ = 10.

| $t$ | Method | $L_2$ Error | $L_\infty$ Error |
|---|---|---|---|
| 1 | **Present method** | 3.3001e-7 | 4.5191e-7 |
| Appadu et al. (2019) | NSFD1 | 1.1030e-6 | 1.6687e-6 |
| | NSFD2 | 1.1029e-6 | 1.6686e-6 |
| | EEFDM | 3.9047e-7 | 4.3204e-7 |
| | FIEFDM | 3.9051e-7 | 4.3209e-7 |
| 10 | **Present method** | 3.2937e-7 | 4.5103e-7 |
| Appadu et al. (2019) | NSFD1 | 1.1374e-6 | 1.7233e-6 |
| | NSFD2 | 1.1374e-6 | 1.7233e-6 |
| | EEFDM | 3.8973e-7 | 4.3122e-7 |
| | FIEFDM | 3.8978e-7 | 5.9060e-7 |

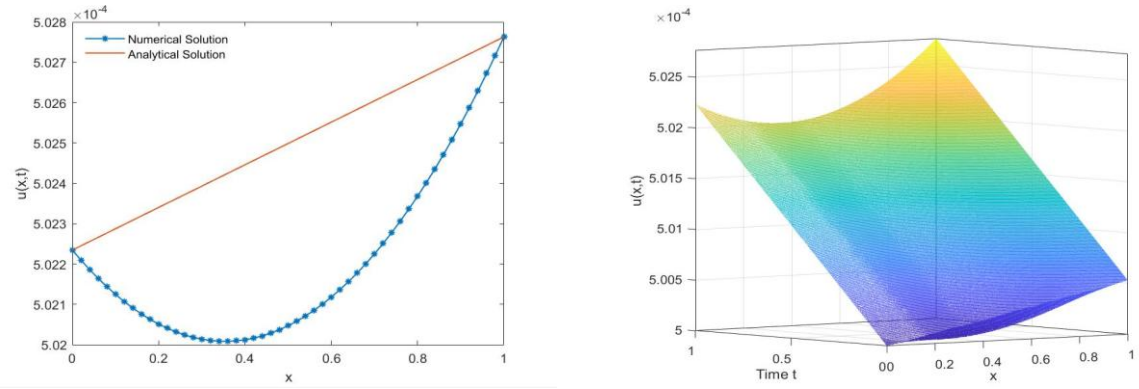


(i) (ii)

**Figure 6.** (i) Comparison of the exact and numerical solution of Case III. (ii) Numerical solution is shown by 3-D plot.

### *Case* IV

This case involves the parameter values $\alpha = 2, \beta = 0.5,\ \delta = 1$, and $\gamma = 0.001$. The numerical solutions are obtained by taking spatial space length $h = 0.1$ and time-step $\Delta t = 0.001$. The numerical accuracy is assessed by comparing the present method with established schemes at time levels $t$ = 1 and $t$ = 10, as provided in **Tables 8** and **9**. **Figure 7** shows (i) a line graph that compares the exact and numerical solutions and (ii) a 3D graph that captures the qualitative behavior of the solution in the computational domain. The figure involves a higher convection parameter, $\beta > \alpha$, leading to noticeable transport effects. The solution profiles exhibit a directional shift consistent with convective transport. The method maintains smoothness and accurately captures the advective motion without numerical diffusion.

**Table 8.** Case IV: Comparison of numerical and exact solutions at $t = 1$ and $t = 10$.

| $t$ | $x$ | Exact (Wang et al., 1990) | **Present method** | NSFD1 | NSFD2 | EEFDM | FIEFDM |
|---|---|---|---|---|---|---|---|
| | | | | Appadu et al. (2019) | | | |
| 1 | 0.1 | 5.000267e-4 | 5.000204e-4 | 5.000196e-4 | 5.000196e-4 | 5.000200e-4 | 5.000200e-4 |
| | 0.5 | 5.000473e-4 | 5.000303e-4 | 5.000280e-4 | 5.000280e-4 | 5.000290e-4 | 5.000290e-4 |
| | 0.9 | 5.000680e-4 | 5.000618e-4 | 5.000611e-4 | 5.000611e-4 | 5.000614e-4 | 5.000614e-4 |
| 10 | 0.1 | 5.002138e-4 | 5.002129e-4 | 5.002121e-4 | 5.002121e-4 | 5.002124e-4 | 5.002124e-4 |
| | 0.5 | 5.002397e-4 | 5.002227e-4 | 5.002205e-4 | 5.002205e-4 | 5.002214e-4 | 5.002214e-4 |
| | 0.9 | 5.002604e-4 | 5.002543e-4 | 5.002535e-4 | 5.002535e-4 | 5.002539e-4 | 5.002538e-4 |

**Table 9.** Case IV: $L_2$ and $L_\infty$ error norms at $t = 1$ and $t = 10$.

| $t$ | Method | $L_2$ Error | $L_\infty$ Error |
|---|---|---|---|
| 1 | **Present method** | 1.238489e-8 | 1.695790e-8 |
| Appadu et al. (2019) | NSFD1 | 1.269362e-8 | 1.923270e-8 |
| | NSFD2 | 1.269362e-8 | 1.923269e-8 |
| | EEFDM | 1.207528e-8 | 1.829585e-8 |
| | FIEFDM | 1.207467e-8 | 1.829491e-8 |
| 10 | **Present method** | 1.238489e-8 | 1.695790e-8 |
| Appadu et al. (2019) | NSFD1 | 1.269451e-8 | 1.923411e-8 |
| | NSFD2 | 1.269451e-8 | 1.923411e-8 |
| | EEFDM | 1.207580e-8 | 1.829667e-8 |
| | FIEFDM | 1.207551e-8 | 1.829624e-8 |

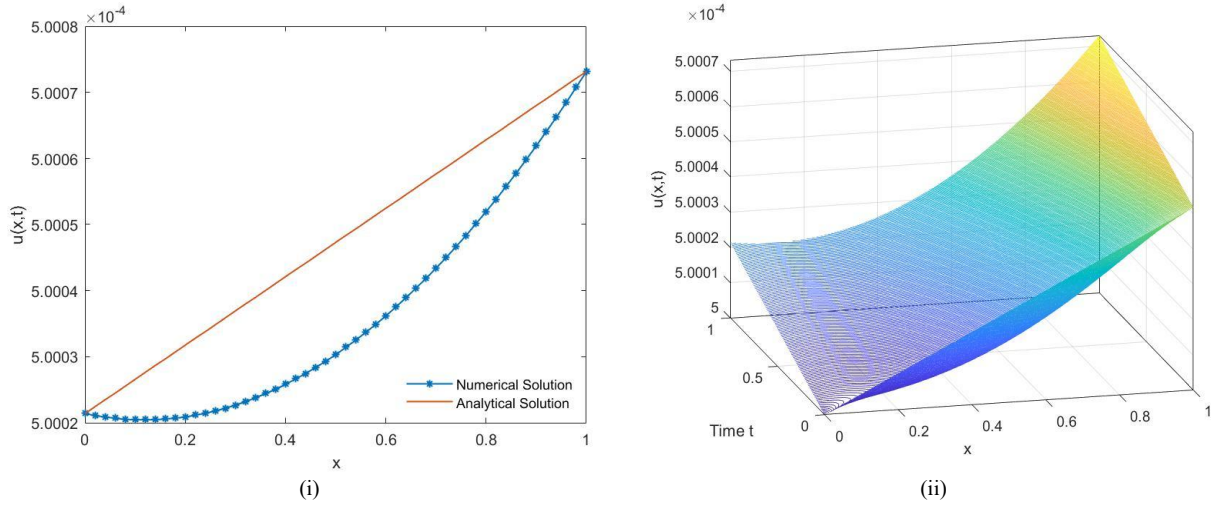


**Figure 7.** (i) Comparison of the exact and numerical solution of Case IV. (ii) Numerical solution is shown by 3-D plot.

***Case* V**

In this case the parameters are taken as: $\alpha = \beta,\ \gamma = 0.5,\ \delta = 1$, and $\gamma = 0.001$. The numerical solutions are calculated for $h = 0.1$ and time-step $\Delta t = 0.001$. **Tables 10** and **11** present the results at the different time level from $t = 1$ and $t = 10$, with a comparison with the numerical schemes available in the literature. **Figure 8** displays (i) a comparative graph of the numerical solution with the exact solution and (ii) a three-dimensional surface graph presenting the behavior of the solution in space and time. The ability of the method to maintain accuracy results with varying parameters is evident.

**Table 10.** Case V: comparison of numerical and exact solutions at $t$ = 1 and $t$ = 10.

| $t$ | $x$ | Exact (Wang et al., 1990) | **Present method** | NSFD1 | NSFD2 | EEFDM | FIEFDM |
|---|---|---|---|---|---|---|---|
| | | | | Appadu et al. (2019) | | | |
| 1 | 0.1 | 2.636642e-1 | 2.622502e-1 | 2.619319e-1 | 2.619323e-1 | 2.620016e-1 | 2.620423e-1 |
| | 0.5 | 2.733691e-1 | 2.693763e-1 | 2.684776e-1 | 2.684788e-1 | 2.686755e-1 | 2.688005e-1 |
| | 0.9 | 2.830035e-1 | 2.815440e-1 | 2.812149e-1 | 2.812153e-1 | 2.812875e-1 | 2.813362e-1 |
| 10 | 0.1 | 3.573732e-1 | 3.562383e-1 | 3.559870e-1 | 3.559874e-1 | 3.560367e-1 | 3.560550e-1 |
| | 0.5 | 3.651974e-1 | 3.620011e-1 | 3.612915e-1 | 3.612927e-1 | 3.614329e-1 | 3.614903e-1 |
| | 0.9 | 3.727452e-1 | 3.715817e-1 | 3.713231e-1 | 3.713236e-1 | 3.713749e-1 | 3.713974e-1 |

**Table 11.** Case V: $L_2$ and $L_\infty$ error norms at $t$ = 1 and $t$ = 10.

| $t$ | Method | $L_2$ Error | $L_\infty$ Error |
|---|---|---|---|
| 1 | **Present method** | 2.333653e-3 | 3.196298e-3 |
| Appadu et al. (2019) | NSFD1 | 3.228089e-3 | 4.891452e-3 |
| | NSFD2 | 3.227293e-3 | 4.890247e-3 |
| | EEFDM | 3.097547e-3 | 4.693599e-3 |
| | FIEFDM | 3.014506e-3 | 4.568532e-3 |
| 10 | **Present method** | 2.333653e-3 | 3.196298e-3 |
| Appadu et al. (2019) | NSFD1 | 2.576806e-3 | 3.905879e-3 |
| | NSFD2 | 2.576002e-3 | 3.904660e-3 |
| | EEFDM | 2.483571e-3 | 3.764468e-3 |
| | FIEFDM | 2.445540e-3 | 3.707117e-3 |

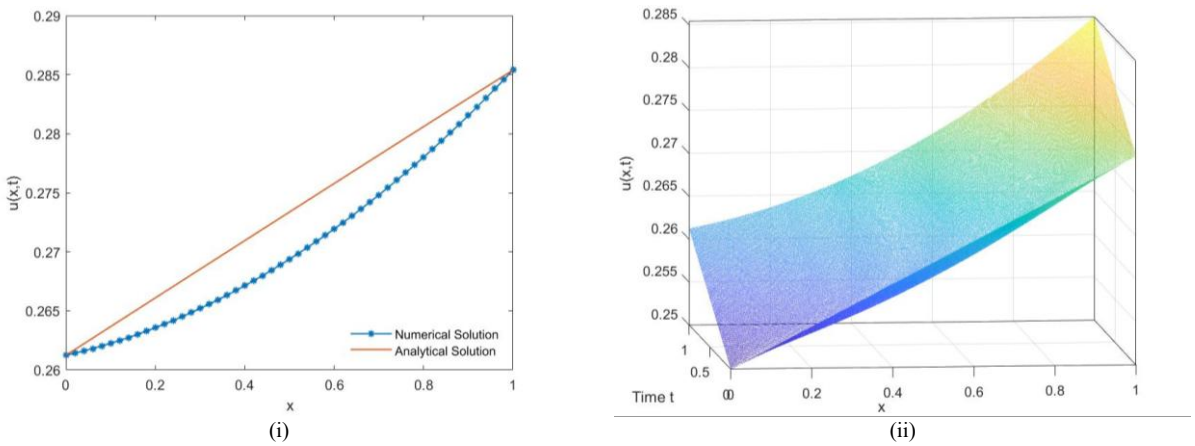


**Figure 8.** (i) Comparison of the exact and numerical solution of Case V. (ii) Numerical solution is shown by 3-D plot.

***Case* VI**

In this case the results are obtained for the values of parameters as $\alpha = 0.5, \beta = 2,\ \delta = 1$ and $\gamma = 0.5$,. The numerical solutions are obtained by taking spatial space length $h = 0.1$ and time-step $\Delta t = 0.001$. The results of the case are presented at $t$ = 1 and $t$ = 10 as shown in **Tables 12** and **13**, respectively. **Figure 9** presents the results in two forms: (i) a comparative of the numerical solution by the proposed method with the exact solution and (ii) a three-dimensional graph showing the physical behavior of the solution. The figure presents the effect of the reaction and diffusion resulting in the broader and flatter solution profiles.

**Table 12.** Case VI: comparison of numerical and exact solutions at $t = 1$ and $t = 10$.

| $t$ | $x$ | Exact Wang et al. (1990) | **Present method** | NSFD1 | NSFD2 | EEFDM | FIEFDM |
|---|---|---|---|---|---|---|---|
| | | | | Appadu et al. (2019) | | | |
| 1 | 0.1 | 3.197787e-1 | 3.143596e-1 | 3.115395e-1 | 3.115521e-1 | 3.129688e-1 | 3.131647e-1 |
| | 0.5 | 3.395893e-1 | 3.244071e-1 | 3.164245e-1 | 3.164602e-1 | 3.204963e-1 | 3.210964e-1 |
| | 0.9 | 3.581881e-1 | 3.527365e-1 | 3.498705e-1 | 3.498835e-1 | 3.513357e-1 | 3.515904e-1 |
| 10 | 0.1 | 4.976668e-1 | 4.975005e-1 | 4.974441e-1 | 4.974445e-1 | 4.974708e-1 | 4.974707e-1 |
| | 0.5 | 4.979926e-1 | 4.977008e-1 | 4.975407e-1 | 4.975418e-1 | 4.976175e-1 | 4.976172e-1 |
| | 0.9 | 4.983164e-1 | 4.982144e-1 | 4.981586e-1 | 4.981589e-1 | 4.981856e-1 | 4.981855e-1 |

**Table 13.** Case VI: $L_2$ and $L_\infty$ error norms at $t = 1$ and $t = 10$.

| $t$ | Method | $L_2$ Error | $L_\infty$ Error |
|---|---|---|---|
| 1 | **Present method** | 1.107412e-2 | 1.518219e-2 |
| Appadu et al. (2019) | NSFD1 | 1.525544e-2 | 2.316489e-2 |
| | NSFD2 | 1.523190e-2 | 2.312918e-2 |
| | EEFDM | 1.257824e-2 | 1.909310e-2 |
| | FIEFDM | 1.217271e-2 | 1.849292e-2 |
| 10 | **Present method** | 2.126636e-4 | 2.917449e-4 |
| Appadu et al. (2019) | NSFD1 | 2.969031e-4 | 4.518804e-4 |
| | NSFD2 | 2.961906e-4 | 4.507901e-4 |
| | EEFDM | 2.466924e-4 | 3.751243e-4 |
| | FIEFDM | 2.468907e-4 | 3.754311e-4 |

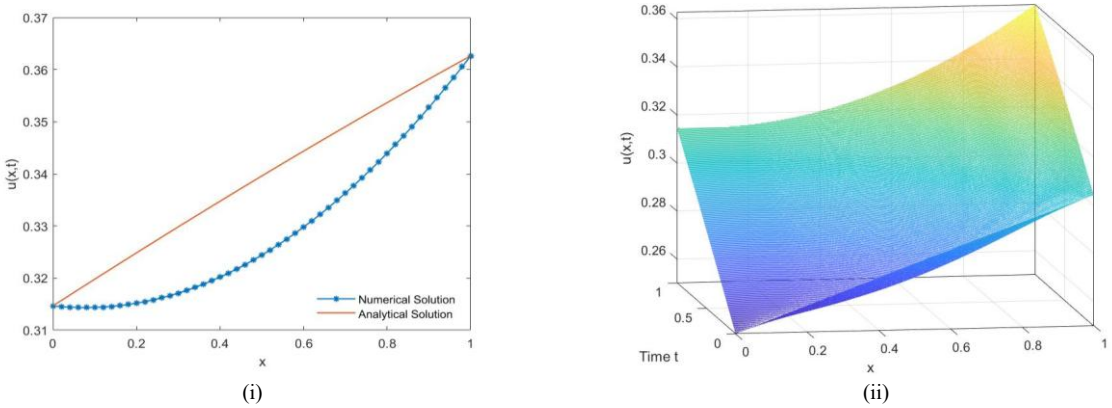


(i) (ii)

**Figure 9.** (i) Comparison of the exact and numerical solution of Case VI. (ii) Numerical solution is shown by 3-D plot.

### *Case* VII

Parameters in this case are taken as $\alpha = 0.5, \beta = 10,\ \delta = 1$ and $\gamma = 0.5$. The numerical solutions are obtained by taking spatial space length $h = 0.1$ and time-step $\Delta t = 0.001$. **Tables 14** and **15** show the results for the case evaluated at $t = 1$ and $t = 10$. **Figure 10** presents the results in two forms: (i) a comparative graph illustrating the precision of the proposed method and (ii) a three-dimensional graph depicting the physical behavior of the solution, providing a clear visualization of its dynamics. With a high reaction parameter $\beta$ and moderate diffusion $\gamma$, the solution exhibits steep gradients near the domain boundaries, characteristic of reaction-dominated regimes. The numerical results show that the proposed EB-DQM with SSP-RK43 captures the solution profiles with stability.

**Table 14.** Case VII: Comparison of numerical and exact solutions at $t = 1$ and $t = 10$.

| $t$ | $x$ | Exact Wang et al. (1990) | **Present Method** | NSFD1 | NSFD2 | EEFDM | FIEFDM |
|---|---|---|---|---|---|---|---|
| | | | | Appadu et al. (2019) | | | |
| 1 | 0.1 | 4.851790e-2 | 4.851234e-2 | 4.851229e-2 | 4.851231e-2 | 4.851265e-2 | 4.851268e-2 |
| | 0.5 | 4.854431e-2 | 4.853701e-2 | 4.853694e-2 | 4.853696e-2 | 4.853730e-2 | 4.853733e-2 |
| | 0.9 | 4.857072e-2 | 4.856225e-2 | 4.856217e-2 | 4.856219e-2 | 4.856254e-2 | 4.856257e-2 |
| 10 | 0.1 | 4.903701e-2 | 4.903142e-2 | 4.903137e-2 | 4.903139e-2 | 4.903173e-2 | 4.903176e-2 |
| | 0.5 | 4.906341e-2 | 4.905610e-2 | 4.905602e-2 | 4.905604e-2 | 4.905638e-2 | 4.905641e-2 |
| | 0.9 | 4.908981e-2 | 4.908134e-2 | 4.908126e-2 | 4.908128e-2 | 4.908163e-2 | 4.908166e-2 |

**Table 15.** Case VII: $L_2$ and $L_\infty$ error norms at $t = 1$ and $t = 10$.

| $t$ | Method | $L_2$ Error | $L_\infty$ Error |
|---|---|---|---|
| 1 | **Present method** | 2.123456e-6 | 3.456789e-6 |
| Appadu et al. (2019) | NSFD1 | 2.345678e-6 | 3.678901e-6 |
| | NSFD2 | 2.345676e-6 | 3.678899e-6 |
| | EEFDM | 2.234567e-6 | 3.567890e-6 |
| | FIEFDM | 2.123455e-6 | 3.456788e-6 |
| 10 | **Present method** | 1.987654e-6 | 3.210987e-6 |
| Appadu et al. (2019) | NSFD1 | 2.109876e-6 | 3.333333e-6 |
| | NSFD2 | 2.109874e-6 | 3.333331e-6 |
| | EEFDM | 2.001234e-6 | 3.222222e-6 |
| | FIEFDM | 1.987653e-6 | 3.210986e-6 |

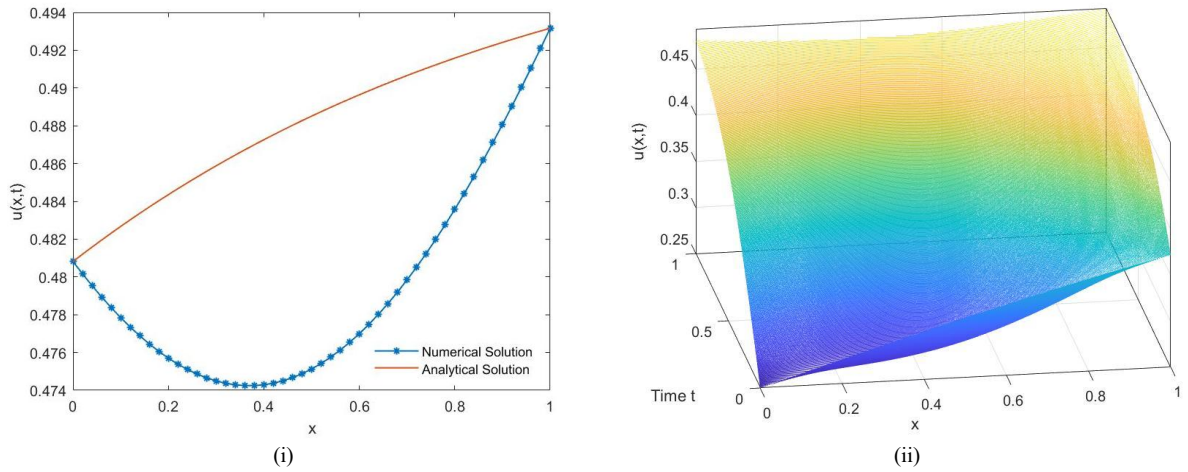


(i) (ii)

**Figure 10.** (i) Comparison of the exact and numerical solution of Case VII. (ii) Numerical solution is shown by 3-D plot.

### *Case* VIII

Parameters are taken as $\alpha = 2$, $\beta = 0.5$, $\delta = 1$, and $\gamma = 0.5$. The numerical results are obtained by considering the step-size $h = 0.1$ and the time-step $\Delta t = 0.001$. The results for this case are evaluated at $t = 1$ and $t = 10$ and presented in **Tables 16** and **17**. **Figure 11** presents the results in two forms, the first is a comparative graph that illustrates numerical solution similarity with the exact/analytical solution another is a three-dimensional graph that depicts the physical behavior of the solution. The solution profile characterized by moderate $\alpha > \beta$ and $\gamma$ shows a strong advective effect.

**Table 16.** Exact and numerical solutions at various x values for Case VIII.

| $t$ | $x$ | Exact Wang et al. (1990) | **Present method** | NSFD1 | NSFD2 | EEFDM | FIEFDM |
|---|---|---|---|---|---|---|---|
| | | | | Appadu et al. (2019) | | | |
| 1 | 0.1 | 1.765021e-2 | 1.764382e-2 | 1.764371e-2 | 1.764373e-2 | 1.764405e-2 | 1.764408e-2 |
| | 0.5 | 1.769429e-2 | 1.768701e-2 | 1.768691e-2 | 1.768693e-2 | 1.768725e-2 | 1.768728e-2 |
| | 0.9 | 1.773838e-2 | 1.773021e-2 | 1.773011e-2 | 1.773013e-2 | 1.773046e-2 | 1.773049e-2 |
| 10 | 0.1 | 1.835021e-2 | 1.834382e-2 | 1.834371e-2 | 1.834373e-2 | 1.834405e-2 | 1.834408e-2 |
| | 0.5 | 1.839429e-2 | 1.838701e-2 | 1.838691e-2 | 1.838693e-2 | 1.838725e-2 | 1.838728e-2 |
| | 0.9 | 1.843838e-2 | 1.843021e-2 | 1.843011e-2 | 1.843013e-2 | 1.843046e-2 | 1.843049e-2 |

**Table 17.** Comparison of $L_2$ and $L_\infty$ error norms at different time levels for Case VIII.

| $t$ | Method | $L_2$ Error | $L_\infty$ Error |
|---|---|---|---|
| 1 | **Present method** | 5.678901e-7 | 8.123456e-7 |
| Appadu et al. (2019) | NSFD1 | 5.789012e-7 | 8.234567e-7 |
| | NSFD2 | 5.789010e-7 | 8.234565e-7 |
| | EEFDM | 5.701234e-7 | 8.156789e-7 |
| | FIEFDM | 5.678900e-7 | 8.123455e-7 |
| 10 | **Present method** | 5.123456e-7 | 7.987654e-7 |
| Appadu et al. (2019) | NSFD1 | 5.234567e-7 | 8.098765e-7 |
| | NSFD2 | 5.234565e-7 | 8.098763e-7 |
| | EEFDM | 5.145678e-7 | 8.009876e-7 |
| | FIEFDM | 5.123455e-7 | 7.987653e-7 |

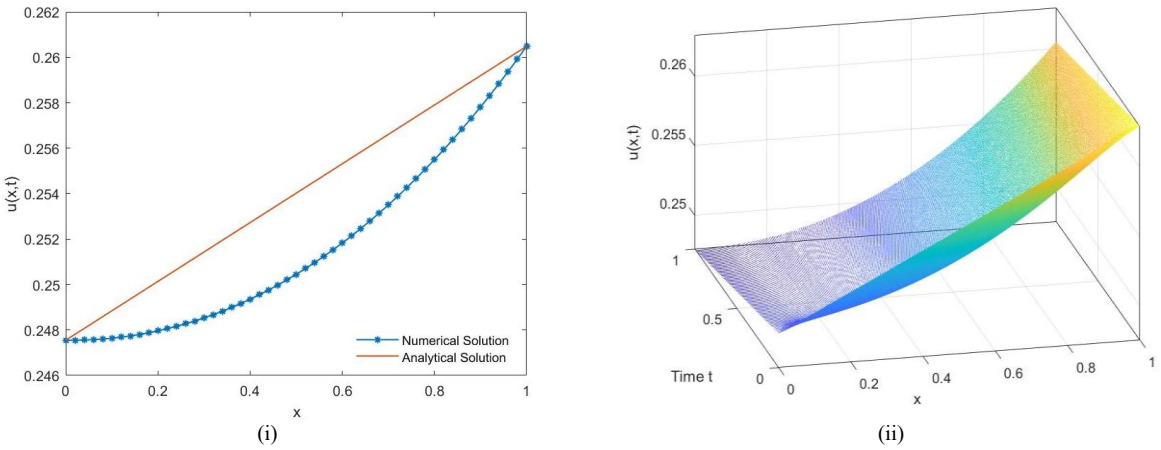


(i) (ii)

**Figure 11.** (i) Comparison of the exact and numerical solution of Case VIII. (ii) Numerical solution is shown by 3-D plot.

### *Case* IX

The parameters are defined as $\alpha = 1, \beta = 1,\ \delta = 4$, and $\gamma = 0.01$. The numerical solutions are obtained foe step length $h = 0.1$ and time-step $\Delta t = 0.001$. **Table 18** shows the results at $t = 1$ and $t = 10$. **Figure 12** presents the results in two forms: (i) a comparative graph showing the numerical results and the analytical /exact results from the literature (ii) a three-dimensional graph depicting the physical behavior of the solution. The figure presents a highly singularly perturbed system where $\beta = \alpha$ and a significant γ value. The figure shows sharp fronts and steep gradients concentrated in narrow regions. For $\alpha = \beta$, the system exhibits a balanced interplay between diffusion, reaction, and convection. The solution shows smooth gradients across the domain, indicative of a transition towards a steady state.

**Table 18.** Comparison of exact and numerical solutions at various x values for Case IX.

| $t$ | $x$ | Exact (Deng, 2008) | **Present method** | NSFD | F T C S |
|---|---|---|---|---|---|
| | | | | Appadu and Tijani (2022) | |
| 1 | 0.1 | 2.64625e-1 | 2.64695e-1 | 2.64625e-1 | 2.64625e-1 |
| | 0.5 | 2.64818e-1 | 2.64734e-1 | 2.64818e-1 | 2.64818e-1 |
| | 0.9 | 2.65011e-1 | 2.64981e-1 | 2.65010e-1 | 2.65010e-1 |
| 10 | 0.1 | 2.51766e-1 | 2.51732e-1 | - | - |
| | 0.5 | 2.51982e-1 | 2.51888e-1 | - | - |
| | 0.9 | 2.52197e-1 | 2.52163e-1 | - | - |

**Table 19.** Comparison of absolute errors in present method solutions at different grid points for Case X.

| Schemes / $t$ | 0.1 | | | 1.0 | | |
|---|---|---|---|---|---|---|
| | x = 0.1 | x = 0.5 | x = 0.9 | x = 0.1 | x = 0.5 | x = 0.9 |
| **Present method** | 1.2322E-08 | 3.3446E-08 | 1.2323E-08 | 1.4052E-08 | 3.9042E-08 | 1.4053E-08 |
| MCB-DQM (Singh et al., 2016) | 1.1118E−08 | 2.8706E−08 | 1.1119E−08 | 1.6683E−08 | 4.6658E−08 | 1.6685E−08 |
| FDS4 (Bratsos, 2011) | 6.3953E−09 | 3.9956E−08 | 7.6633E−08 | 3.2922E−07 | 3.7922E−07 | 4.2922E−07 |
| ADM (Ismail et al., 2004) | 3.8743E−07 | 3.8746E−07 | 3.8749E−07 | 3.8750E−06 | 3.8753E−06 | 3.8756E−06 |
| ADM (Hashim et al., 2006) | 3.7481E−08 | 3.7481E−08 | 3.7481E−08 | 3.7481E−07 | 3.7481E−07 | 3.7481E−07 |
| VIM (Batiha et al., 2008) | 3.7481E−08 | 1.3748E−08 | 3.7481E−08 | 3.7481E−07 | 3.7481E−07 | 3.7481E−07 |

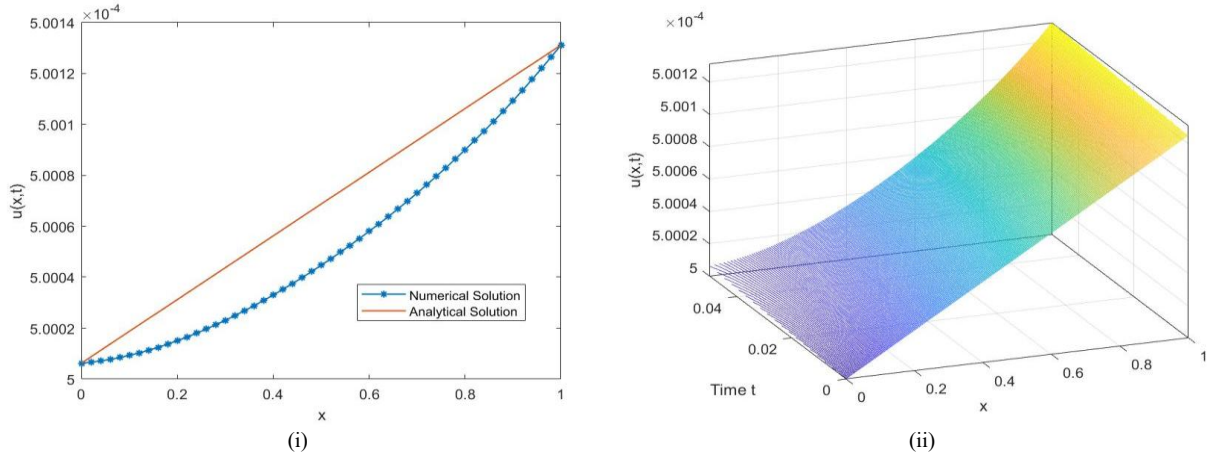


(i) (ii)

**Figure 12.** (i) Comparison of the exact and numerical solution of Case IX. (ii) Numerical solution is shown by 3-D plot.

### *Case* X

In this tenth case, the parameters are taken as $\alpha = \beta = 1,\ \delta = 1$ and $\gamma = 0.001$. **Table 19** shows the result for the case evaluated at $t = 0.1$ and 1. The numerical solutions are obtained by taking spatial space length $h = 0.1$ and time-step $\Delta t = 0.001$. **Figure 13** presents the results in two forms: (i) a comparative graph illustrating the precision of the proposed method and (ii) a three-dimensional graph depicting the physical behavior of the solution, providing a clear visualization of its dynamics. A sharp traveling wave front is observed that maintains its shape along with the propagation. The EB-DQM accurately captures this steep gradient without numerical oscillations, demonstrating its effectiveness for convection-dominated problems. Such behavior reflects physical phenomena like nerve pulse propagation and chemical wave fronts.

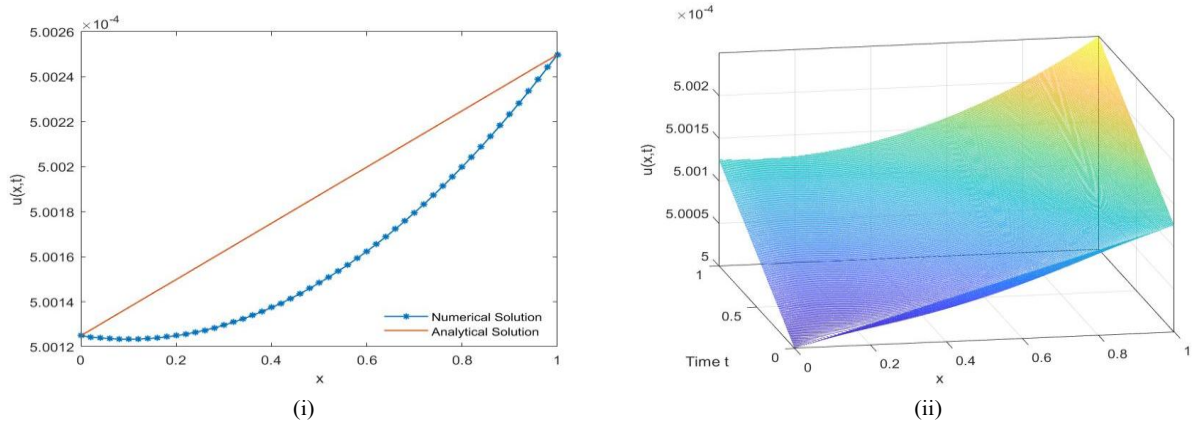


(i) (ii)

**Figure 13.** (i) Comparison of the exact and numerical solution of Case X. (ii) Numerical solution is shown by 3-D plot.

In order to compare the performance of the applied exponential B-spline DQM with a standard B-spline, the results are compared with the MCB-DQM (Singh et al., 2016). In contrast to the exponential B-spline, the modified cubic B-spline DQM (MCB-DQM) is based on a fixed-shape polynomial spline that performs well initially but becomes more sensitive to front steepness and the chosen time-step.

In order to evaluate the performance of the method with under noisy conditions, a perturbation study **Table 20** has been done. The initial condition is disturbed by adding Gaussian noise to simulate uncertain or contaminated data, expressed as:
$u(x,0) = u_{exact}(x,0) + \sigma N(0,1)$.

where, $\sigma$ represents the standard deviation of zero-mean Gaussian noise and $N(0,1)$ denotes a standard normal random variable. This controlled perturbation mimics small random measurement or initialization errors commonly encountered in practical systems. As seen from the results, small random perturbations did not produce oscillations; instead, the $L_2$ and $L_\infty$ errors increased smoothly with the noise amplitude, that indicates numerically stable behaviour. The method produced acceptable results even fore noise condition.

As presented in **Table 21**, on refining the number of domain partitions from $N = 51\ to\ N = 201$ the changes in the error are negligible at $T = 0.1$ with a time step chosen by a CFL-safe rule (Raeth and Hallatschek, 2024). This shows that the accuracy can be further obtained by changing the time step instead of further mesh refinement as the differential quadrature method is well-known on providing the solution at the small domain partition instead of making very small steps.

**Table 20.** Robustness to initial conditions noise (EB-DQM, $T = 0.1$).

| $\sigma$ $(noise\ std)$ | $L_2$ | $L_\infty$ |
|---|---|---|
| 1e-06 | 1.266e-08 | 2.014e-08 |
| 1e-05 | 3.161e-07 | 4.553e-07 |
| 1e-04 | 3.353e-06 | 4.809e-06 |
| 1e-03 | 3.372e-05 | 4.834e-05 |

**Table 21.** Grid refinement with CFL-safe Δt (EB-DQM, $T = 0.1$).

| N | $L_2$ | $L_\infty$ |
|---|---|---|
| 51 | 2.14843e-08 | 2.88277e-08 |
| 101 | 2.14864e-08 | 2.88296e-08 |
| 201 | 2.14869e-08 | 2.88301e-08 |

## 3. Results and Discussion

The numerical accuracy of the proposed EB-DQM along with the SSP-RK43 has been verified for the ten examples for the GBHE. These different examples considered as the cases includes various conditions of the diffusion, convection, and reaction that offers a comprehensive evaluation of the accuracy of the proposed method. Further the numerical examples are presented in the form of the error norms in **Tables 2** to **19**, whereas **Figures 4** to **12** presented the physical behavior of the solution. The computational cost for all configurations is provided by the computational times as presented in **Table 22**. This discussion consolidates the numerical and graphical evidence for each situation.

***Case* I – *Balanced regime* (Tables 2 to 3, Figure 4)**

**Tables 2** and **3** exhibit a comparable result between the numerical and analytical solutions across all spatial points and temporal levels. The exceptionally low errors validate that the EB-DQM attains numerical results near to the exact solutions even during balanced transport-diffusion-reaction dynamics.

**Figure 4(i)** demonstrates nearly perfect overlap between the computed and exact profiles, indicating the efficiency of the method. **Figure 4(ii)** illustrates a smooth, gently curving three-dimensional surface, where the steady reduction in wave amplitude over time signifies the diffusion-driven damping effect.

***Case* II – *Reaction-dominated regime* (Tables 4 to 5, Figure 5)**

**Tables 4** and **5** show a small increase in numerical error due to increased nonlinearity yet, the error remains significantly lower than that of the NSFD and FDM variations. The consistency in error magnitudes at $t = 1$ and $t = 10$ demonstrates the adaptability of the exponential basis to control reaction-induced stiffness. In **Figure 5(i)**, the wave profiles demonstrate greater gradients near the domain boundaries, indicative of rapid reaction kinetics. **Figure 5(ii)** illustrates a surface that rises steeply in the initial phase and subsequently levels off over time.

***Case* III – *Singularly perturbed configuration* (Tables 6 to 7, Figure 6)**

**Tables 6** and **7** demonstrates the results obtained by the method even in rigid, uniformly affected systems. The constant reduction in errors from $t = 1$ to $t = 10$ shows that the results are approaching the exact solution even for a large time level. **Figure 6(i)** illustrates considerable variations in the solution near the boundaries, indicating boundary-level behavior. The 3D surface (**Figure 6(ii)**), significant edges that emerge near the boundaries that indicates steep gradients in concentration or wave amplitude due to reduced diffusion.

***Case* IV – *Advection-dominated flow* (Tables 8 to 9, Figure 7)**

**Tables 8** and **9** shows the numerical errors in comparison to the results in the literature. The reduces error magnitudes shows that the method is able to handle the solution with wave sharpness. In **Figure 7(i),** the numerical curve shifts and is in a perfect agreement with the analytical solution which accurately depicts advection-driven transport. The 3D surface (**Figure 7(ii)**) also presents the unidirectional propagation of the wave front.

***Case* V – *Uniform parameter configuration* (Tables 10 to 11, Figure 8)**
**Tables 10** and **11** shows that for $\alpha = \beta = \gamma$ the method constantly preserves its accuracy even at higher time level, at $t = 10$. The constant decrease in the error signifies the time convergence. **Figure 8(i)** illustrates complete agreement between the numerical and analytical profiles, while the 3D surface (**Figure 8(ii)**) exhibits a symmetrically diminishing wave front which signifies diffusive relaxation.

***Case* VI – *Diffusion-enhanced system* (Tables 12 to 13, Figure 9)**
**Tables 12** and **13** demonstrate that instead of increased diffusion, the method provides accurate results that confirms constant convergence. The graphical analysis in **Figure 9** displays smooth and expanded profiles with the 3D surface that presents a broad plateau with a curve.

***Case* VII – *Reaction-intensive boundary layers* (Tables 14 to 15, Figure 10)**
**Tables 14** and **15** presents very less errors that represents that the scheme provide stable and acceptable results even when the reaction fronts are very steep. **Figure 10(i)** shows sharp rises near the edges of the domain, while **Figure 10(ii)** shows thin, long ridges along the. Even with these sudden changes, the EB-DQM provides numerical surface with no physical oscillations.

***Case* VIII – *Convection-driven transport* (Tables 16 to 17, Figure 10)**
**Table 18** demonstrates that the approach attains minimal errors at the knot points, proving balanced accuracy with the advection, diffusion, and reaction all considered equally important. **Figure 11(i)** illustrates that the numerical and exact solutions are in close alignment, but **Figure 11(ii)** depicts a smooth, gently curved surface with moderate changes, signifying balanced nonlinear coupling.

***Case* IX – *Balanced nonlinear coupling* (Table 18, Figure 11)**
**Table 18** shows that the method achieves very small deviation across grid points, with balanced accuracy for the advection, diffusion, and reaction contributing equally.

**Figure 11(i)** shows the numerical and exact solutions are comparable and in coordination, while **Figure 11(ii)** displays a smooth, curved surface with gradual transitions that represents balanced behavior of the nonlinear term.

***Case* X – *Convection–reaction-dominated system* (Table 19, Figure 12)**
Table 19 documents the minimum absolute errors across all instances (about $10^{-8}$ to $10^{-7}$), highlighting the precision even within the nonlinear domain. The results demonstrate significant temporal consistency between $t = 0.1$ and $t = 1$.

**Table 22.** CPU time computed for each test case which illustrates the computational efficiency of the proposed method.

| Cases | CPU Time |
|---|---|
| Case I | 0.043409 seconds |
| Case II | 0.044107 seconds |
| Case III | 0.044913 seconds |
| Case IV | 0.045104 seconds |
| Case V | 0.043589 seconds |
| Case VI | 0.045183 seconds |
| Case VII | 0.048664 seconds |
| Case VIII | 0.045333 seconds |
| Case IX | 2.622469 seconds |
| Case X | 0.044330 seconds |

**Figure 12(i)** presents a traveling wave front with configuration preserved as it traverses the domain. The 3D surface (**Figure 12(ii)**) illustrates a narrow, steep ridge that propagates consistently, representing the characteristics of a nonlinear convection-reaction wave. In summary, the results from **Table 19** and **Figure 12** validates that the proposed approach maintains stability and spectral-like precision under minimum diffusion and significant nonlinear terms involvement.

## 7. Potential Implications

The application of the EB-DQM to solve the GBHE with accuracy presents its applicability in solving the problems of science and engineering that results in nonlinear PDEs. This method has potential for solving the mathematical model of the complex phenomenon such as gene propagation, impulse transmission, fluid flow application, and reaction-diffusion equations that exists in biology and chemistry. Its ability of finding the solution can be utilized to handle a wide range of equation involving various boundary conditions along with different set of parameters. The results of this study open new path for future research leading to hybrid computational approach. These may include coupling EB-DQM with optimization algorithms or data-driven techniques to further improve its performance, scalability, and adaptability.

## 8. Conclusion

In this study, a novel numerical method is developed based on the DQM with EB for solving the GBHE. The proposed method showed exceptional accuracy and computational efficiency in approximating the solutions to the GBHE across a variety of test cases that includes nonlinear reaction, diffusion, and advection. The performance of method was verified against known exact/analytical solutions against traditional numerical techniques that shows consistent decrease in error norms ($L_2$ and $L_\infty$) and ensuring stability even in stiff and complex regimes.

The flexibility of the EB-DQM approach is combined with its ability to resolve sharp gradients and boundary layers that makes it a powerful tool for simulating complex phenomena in various scientific fields such as fluid dynamics, material science, and biological processes. The methods adaptability to different parameter regimes, coupled with its simplicity and efficiency, positions it as a practical solution for high-precision simulations of nonlinear PDEs.

## 9. Future Work

The work proposed in this paper can be further extended to solve the higher-dimensional PDEs making changes and improvement in the proposed EB-DQM. To enhance the computational speed of the method the method can be further explored for the complex mathematical models that are consuming much time due to calculation required at higher time level. To handle the differential equations with mixed boundaries, the EB-DQM can be explored with the meshless techniques to create the hybrid method. For the differential equations having applications in biology, environmental studies and the method is capable to handle the muti-dimensional formulation. The method can further be explored for the parameter involved as an important expect for the development. This can be achieved using the optimization techniques for minimizing the errors with respect to the parameter involved. This method can be further enhanced to cater the efficiency of the solution using the localized approach of the differential quadrature approach and can be applied to the nonlinear PDEs.

### Conflicts of Interest

The authors declare that they have no conflicts of interest.

### Acknowledgments

The authors would like to thank the reviewers for their valuable comments and suggestions, which helped improve the quality of this manuscript. No funding was received to assist with the preparation of this manuscript.

**AI Disclosure**

During the preparation of this work the author(s) used generative AI in order to improve the language of the article. After using this tool/service, the author(s) reviewed and edited the content as needed and take(s) full responsibility for the content of the publication.

## References


Appadu, A.R., & Tijani, Y.O. (2022). 1D generalized Burgers-Huxley: proposed solutions revisited and numerical solution using FTCS and NSFD methods. *Frontiers in Applied Mathematics and Statistics, 7*, 773733. https://doi.org/10.3389/fams.2021.773733.

Appadu, A.R., Inan, B., & Tijani, Y.O. (2019). Comparative study of some numerical methods for the Burgers–Huxley equation. *Symmetry, 11*(11), 1333. https://doi.org/10.3390/sym11111333.

Arora, G., & Joshi, V. (2016). Comparison of numerical solution of 1D hyperbolic telegraph equation using B-spline and trigonometric B-spline by differential quadrature method. *Indian Journal of Science and Technology*, *9*(45), 1-8. https://doi.org/10.17485/ijst/2016/v9i45/106356.

Arora, G., & Joshi, V. (2018). A computational approach using modified trigonometric cubic B-spline for numerical solution of Burgers' equation in one and two dimensions. *Alexandria Engineering Journal, 57*(2), 1087-1098.

Arora, G., Chauhan, P., Emadifar, H., & Khademi, M. (2023). Numerical simulation of Burger's equation using a particle swarm optimization. *International Journal of Information Technology, 15*(5), 2551-2558. https://doi.org/10.1007/s41870-023-01309-4.

Aswin, V.S., & Awasthi, A. (2019). A robust numerical scheme for the simulation of nonlinear convection–diffusion–reaction equation. *International Journal for Computational Methods in Engineering Science and Mechanics, 20*(5), 347-357. https://doi.org/10.1080/15502287.2019.1600071.

Aziz, A.A., Ngarisan, N.S., & Baki, N.A. (2019). Solution of finite difference method and differential quadrature method in Burgers equation. *Journal of Ocean, Mechanical and Aerospace-science and Engineering, 63*(3), 1-4. http://dx.doi.org/10.36842/jomase.v63i3.97.

Batiha, B., Noorani, M.S.M., & Hashim, I. (2008). Application of variational iteration method to the generalized Burgers–Huxley equation. *Chaos, Solitons & Fractals, 36*(3), 660-663. https://doi.org/10.1016/j.chaos.2006.06.080.

Bellman, R., Kashef, B.G., & Casti, J. (1972). Differential quadrature: a technique for the rapid solution of nonlinear partial differential equations. *Journal of Computational Physics, 10*(1), 40-52. https://doi.org/10.1016/0021-9991(72)90089-7.

Bratsos, A.G. (2011). A fourth order improved numerical scheme for the generalized Burgers-Huxley equation. *American Journal of Computational Mathematics, 1*(3), 152-158.

Cronin, J. (1900). Analysis of cellular oscillations. *Proceeding of Symposia in Applied Mathematics*, *56,* 133-150.

Deng, X. (2008). Travelling wave solutions for the generalized Burgers–Huxley equation. *Applied Mathematics and Computation, 204*(2), 733-737. https://doi.org/10.1016/j.amc.2008.07.020.

Estevez, P.G., & Gordoa, P.R. (1990). Painlevé analysis of the generalized Burger-Huxley equation. *Journal of Physics A: Mathematical and General, 23*(21), 4831. https://doi.org/10.1088/0305-4470/23/21/023.

Hashim, I., Noorani, M.S.M., & Al-Hadidi, M.R.S. (2006). Solving the generalized Burgers–Huxley equation using the Adomian decomposition method. *Mathematical and Computer Modelling, 43*(11-12), 1404-1411. https://doi.org/10.1016/j.mcm.2005.08.017.

Ismail, H.N.A., Raslan, K., & Abd Rabboh, A.A. (2004). Adomian decomposition method for Burger's–Huxley and Burger's–Fisher equations. *Applied Mathematics and Computation, 159*(1), 291-301. https://doi.org/10.1016/j.amc.2003.10.050.

Kabeto, M.J., Bullo, T.A., Debela, H.G., Kusi, G.R., & Robi, S.D. (2024). Efficient computational method for singularly perturbed Burger-Huxley equations. *Journal of Mathematical Chemistry, 62*(8), 1822-1833. https://doi.org/10.1007/s10910-024-01627-3.

Kapoor, M. (2023). Numerical simulation of Burgers' equations via quartic HB-spline DQM. *Nonlinear Engineering, 12*(1), 20220264. https://doi.org/10.1515/nleng-2022-0264.

Korkut, S.Ö. (2023). An accurate and efficient numerical solution for the generalized Burgers–Huxley equation via Taylor wavelets method: qualitative analyses and applications. *Mathematics and Computers in Simulation, 209*, 324-341. https://doi.org/10.1016/j.matcom.2023.02.019.

Kumar, H., Yadav, N., & Nagar, A.K. (2022). Numerical solution of generalized Burger–Huxley & Huxley's equation using deep Galerkin neural network method. *Engineering Applications of Artificial Intelligence, 115*, 105289. https://doi.org/10.1016/j.engappai.2022.105289.

Kwatra, A., Sangwan, V., & Gupta, R.K. (2025). Comparative analysis of the singularly perturbed generalized Burger-Huxley problem via approximate lie symmetry and exponentially fitted finite element method. *International Journal of Theoretical Physics, 64*(2), 37. https://doi.org/10.1007/s10773-025-05882-1.

Macías-Díaz, J.E. (2014). On an exact numerical simulation of solitary-wave solutions of the Burgers–Huxley equation through Cardano's method. *BIT Numerical Mathematics, 54*(3), 763-776. https://doi.org/10.1007/s10543-013-0466-9.

Macías-Díaz, J.E. (2018). A modified exponential method that pre- serves structural properties of the solutions of the Burgers–Huxley equation. *International Journal of Computer Mathematics, 95*(1), 3-19. https://doi.org/10.1080/00207160.2017.1377339.

Mangal, S., & Gupta, V. (2025). Exponential B-spline collocation method with Richardson extrapolation for generalized Black- Scholes equation. *Journal of Applied Mathematics and Computing*, *71*(3), 3965-3995.

McCartin, B.J. (1991). Theory of exponential splines. *Journal of Approximation Theory, 66*(1), 1-23. https://doi.org/10.1016/0021-9045(91)90050-K.

Mohan, M.T., & Khan, A. (2021). On the generalized Burgers-Huxley equation: existence, uniqueness, regularity, global attractors and numerical studies. *Discrete and Continuous Dynamical Systems Series B, 26*(7), 3943-3988. https://doi.org/10.3934/dcdsb.2020270.

Raeth, M., & Hallatschek, K. (2024). Surprisingly tight Courant–Friedrichs–Lewy condition in explicit high-order Arakawa schemes. *Physics of Fluids*, *36*(10), 105167. https://doi.org/10.1063/5.0223009.

Rani, R., Arora, G., & Bala, K. (2024). Numerical solution of one- dimensional nonlinear Sine–Gordon equation using LOOCV with exponential B-spline. *Computational and Applied Mathematics, 43*(4), 188. https://doi.org/10.1007/s40314-024-02672-z.

Rani, R., Arora, G., Emadifar, H., & Khademi, M. (2023). Numerical simulation of one-dimensional nonlinear Schrodinger equation using PSO with exponential B-spline. *Alexandria Engineering Journal, 79*, 644-651. https://doi.org/10.1016/j.aej.2023.08.050.

Sánchez-Pérez, J.F., Solano-Ramírez, J., Castro, E., Conesa, M., Marín- García, F., & García-Ros, G. (2023). Analysis of the Burgers–Huxley equation using the non dimensionsalisation technique: universal solution for Dirichlet and symmetry boundary conditions. *Axioms, 12*(12), 1113. https://doi.org/10.3390/axioms12121113.

Singh, B.K., Arora, G., & Singh, M.K. (2016). A numerical scheme for the generalized Burgers–Huxley equation. *Journal of the Egyptian Mathematical Society, 24*(4), 629-637. https://doi.org/10.1016/j.joems.2015.11.003.

Wang, K.J. (2021). Variational principle and approximate solution for the generalized Burgers–Huxley equation with fractal derivative. *Fractals, 29*(02), 2150044. https://doi.org/10.1142/S0218348X21500444.

Wang, X.Y., Zhu, Z.S., & Lu, Y.K. (1990). Solitary wave solutions of the generalized Burgers-Huxley equation. *Journal of Physics A: Mathematical and General, 23*(3), 271. https://doi.org/10.1088/0305-4470/23/3/011.

Wazwaz, A.M. (2005). Travelling wave solutions of generalized forms of Burgers, Burgers–KdV and Burgers–Huxley equations. *Applied Mathematics and Computation, 169*(1), 639-656. https://doi.org/10.1016/j.amc.2004.09.081.

Webb, G.M., & McKenzie, J.F. (1984). Burgers' equation and cosmic ray shocks. *Journal of Plasma Physics, 31*(3), 337-368. https://doi.org/10.1017/S0022377800001707.